

BIRADS Features-Oriented Semi-supervised Deep Learning for Breast Ultrasound Computer-Aided Diagnosis

Erlei Zhang, Stephen Seiler, Mingli Chen, Weiguo Lu, Xuejun Gu

Abstract—Breast ultrasound (US) is an effective imaging modality for breast cancer detection and diagnosis. US computer-aided diagnosis (CAD) systems have been developed for decades and have employed either conventional hand-crafted features or modern automatic deep-learned features, the former relying on clinical experience and the latter demanding large datasets. In this paper, we have developed a novel BIRADS-SDL network that integrates clinically-approved breast lesion characteristics (BIRADS features) into semi-supervised deep learning (SDL) to achieve accurate diagnoses with a small training dataset. Breast US images are converted to BIRADS-oriented feature maps (BFMs) using a distance-transformation coupled with a Gaussian filter. Then, the converted BFMs are used as the input of an SDL network, which performs unsupervised stacked convolutional auto-encoder (SCAE) image reconstruction guided by lesion classification. We trained the BIRADS-SDL network with an alternative learning strategy by balancing reconstruction error and classification label prediction error. We compared the performance of the BIRADS-SDL network with conventional SCAE and SDL methods that use the original images as inputs, as well as with an SCAE that use BFMs as inputs. Experimental results on two breast US datasets show that BIRADS-SDL ranked the best among the four networks, with classification accuracy around $92.00 \pm 2.38\%$ and $83.90 \pm 3.81\%$ on two datasets. These findings indicate that BIRADS-SDL could be promising for effective breast US lesion CAD using small datasets.

Index Terms—Breast cancer; ultrasound; computer-aided diagnosis; BIRADS features; semi-supervised deep learning.

I. INTRODUCTION

Breast cancer is the most common malignancy in women in the United States and the second leading cause of cancer death for women worldwide [1]. Early detection and diagnosis are key to improving patient survival and quality of life, as they provide early and flexible treatment options [2]. Breast ultrasound (US) is a widely adopted early breast cancer

diagnosis imaging modality that has the advantages of being non-invasive, safe, efficient, and relatively inexpensive [3, 4]. However, the main limitation of breast US is operator dependence [5]. Many studies have applied computer-aided diagnosis (CAD) to breast US to assist radiologists and improve diagnostic accuracy [6].

In general, an US CAD system consists of four phases: image preprocessing, lesion segmentation, feature extraction, and classification. Image preprocessing is mainly designed for denoising and contrast enhancement. Segmentation focuses on separating the lesion region from the background and other tissue [7, 8]. Feature extraction abstracts clinical characteristics from the segmented lesion, and classification utilizes the extracted features to differentiate benign from malignant lesions. In traditional US CAD systems, most of the features are hand-crafted [9, 10], considering radiomic, morphologic, and pathologic knowledge. Such feature extraction relies on clinical experience, and extracted features might not be robust in general. Over the years, clinical practice has accumulated knowledge regarding lesion characteristics for manual classification, which could be powerful for accurate diagnosis if incorporated into CAD. The Breast Imaging Reporting and Data System (BIRADS) was proposed by the American College of Radiology to help radiologists consistently describe and evaluate clinical lesions [11]. Descriptive terms of BIRADS features are clinically-approved lesion characteristics designed to quantify lesions by shape, contour attributes, internal echo patterns, and the architecture of the surrounding tissues.

In recent years, deep learning (DL) methods have shown promising performance in computer vision [12-16]. DL-based methods not only support automatically representative and discriminative feature learning, but they also enable unsupervised feature learning [13]. DL has been increasingly adopted in medical image analysis in the past few years [17-19]. Deep convolutional neural networks (CNN) have been used successfully for image segmentation [20] and classification [21] tasks to achieve state-of-the-art performance. DL has also been applied in breast US diagnosis. Cheng *et al.* [22] utilized unsupervised deep stacked auto-encoder (AE)-based methods to extract high-level features and supervised fine-tuning for breast US image classification. Han *et al.* [23] utilized the GoogLeNet pre-trained on gray

This work was supported by a seed grant from Department of Radiation Oncology at the University of Texas Southwestern Medical Center.

E. Zhang is with Northwest University, China, and the Department of Radiation Oncology, UT Southwestern Medical Center, Dallas, TX, USA (e-mail: Erlei.Zhang@UTSouthwestern.edu).

S. Seiler is with the Department of Radiology, UT Southwestern Medical Center, Dallas, TX, USA (e-mail: Stephen.Seiler@UTSouthwestern.edu).

M. Chen, W. Lu, and X. Gu are with the Department of Radiation Oncology, UT Southwestern Medical Center, Dallas, TX, USA (e-mail: {Mingli.Chen, Weiguo.Lu, Xuejun.Gu} @UTSouthwestern.edu).

natural images to classify breast US images with high accuracy. Antropova *et al.* [24] used ImageNet-pretrained CNNs to extract and pool low- to mid-level features and combine them with hand-crafted features to achieve accurate diagnoses on three imaging modality datasets. Most of those DL approaches require large amounts of data to train the models, whereas the pre-training strategy is designed for situations in which data are limited. However, the pre-training strategy faces challenges associated with the differences between the statistics of natural images and US images. Overall, DL has shown promising performance with automatic feature learning, but these approaches suffer from limited datasets to learn and inefficient utilization of accumulated clinical knowledge.

In this paper, we report a novel BIRADS-SDL network (architecture shown in Fig. 1) that incorporates the clinical knowledge of lesion characteristics (BIRADS features) and a task-oriented semi-supervised deep learning (SDL) method to achieve accurate diagnosis on breast US images. The breast US images are converted to BIRADS-oriented feature maps (BFMs) using a distance-transformation coupled Gaussian filter. The BFMs not only keep the original US image

information, but they also enhance the shape, lesion boundary, echo pattern, undulation, and angular characteristics of the lesion. Then, the BFMs are used as the input of an SDL network, which performs a multi-task learning by integrating stacked convolutional auto-encoder (SCAE)-based unsupervised image feature extraction and diagnosis-oriented supervised lesion classification. This integrated multi-task learning allows SCAE to extract image features with the constraints from the lesion classification task, while the lesion classification is achieved by utilizing the SCAE encoder features with a convolutional network. The entire BIRADS-SDL network is trained with an alternative learning strategy by balancing the reconstruction error and classification label prediction error.

The paper is organized as follows: the proposed BIRADS-SDL network is detailed in Section II. Section III details the experimental setup. Then, the proposed method's effectiveness is demonstrated by experimental results in Section IV. Finally, Section V provides a summary and closing remark.

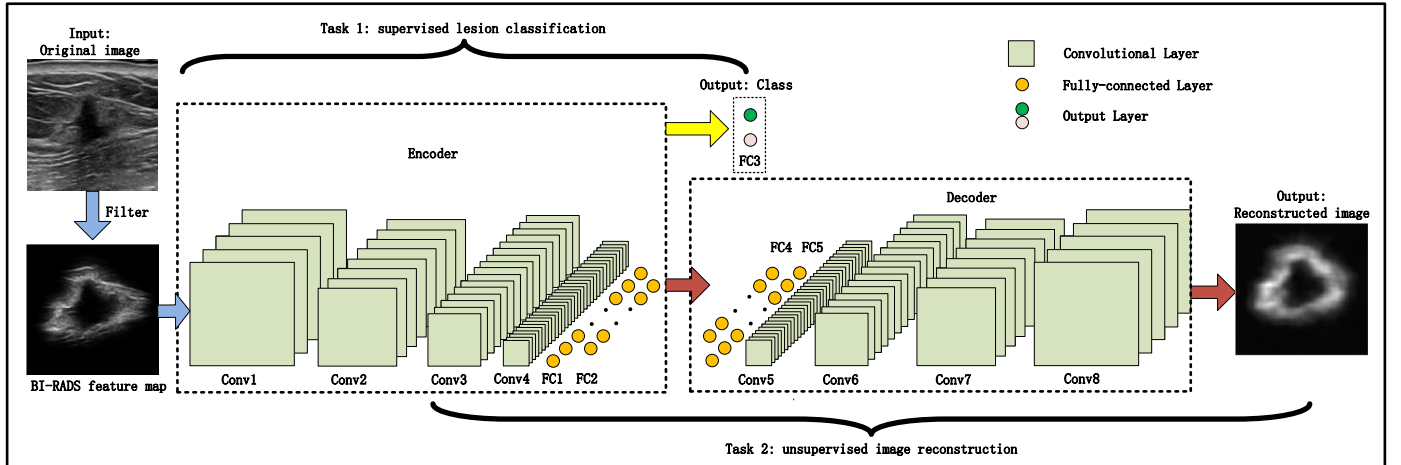


Fig. 1. Illustration of BIRADS-SDL architecture, which consists of BIRADS feature map extraction and an SDL network. The SDL network integrates SCAE-based unsupervised image feature extraction with diagnosis-oriented supervised lesion classification.

II. METHOD

A. BIRADS Features

BIRADS features consist of shape, orientation, margin, lesion boundary, echo pattern, and posterior acoustic feature classes [9], which help radiologists grade the clinical findings, and evaluate their reliability against the pathological results. Fig. 2(a) shows a sample US image with the lesion boundary marked. The undulation and angular characteristics of the lesion, shown in Fig. 2(b), are two important BIRADS features for differentiating benign from malignant lesions. An undulation feature can be expressed as the number of significant lobulated areas partitioned between the lesion boundary and its maximum inscribed circle (blue circle). The angular characteristics can be detected through the local maxima (green dotted line) in each lobulated area on the

distance map. In addition, the abrupt degree characteristic is usually calculated by the average gray intensities between the surrounding tissue and the lesion exterior, as shown in Fig. 2(c).

B. BIRADS-oriented Feature Maps

In this paper, we converted original breast US images to BFMs using a distance-transformation coupled Gaussian filter $DTGF(\cdot)$ to explicitly use these characteristics in DL methods. $DTGF(\cdot)$ is defined as

$$DTGF(p) = e^{-\frac{Dist(p)^2}{\sigma^2}} \quad (1)$$

where the distance transform $Dist(p) = \min\{ED(p, q_i)\}$ represents the Euclidean distance between the image pixel p and boundary pixel q_i . An example of a distance map represented by grayscale is shown in Fig. 2(d). σ is used to control the width of the region of surrounding tissue and the

exterior lesion across the boundary. The **DTGF** assigns different weights based on the distance of the pixel to the boundary and promotes attention to key areas. An example of **DTGF** with $\sigma = 20$ is shown in Fig. 2(e).

With **DTGF**, original breast US images I are converted to BFM as follow:

$$BFMs = I \cdot e^{-\frac{Dist(p)^2}{\sigma^2}} \quad (2)$$

An example of BFM is shown in Fig. 2(f). From the figure,

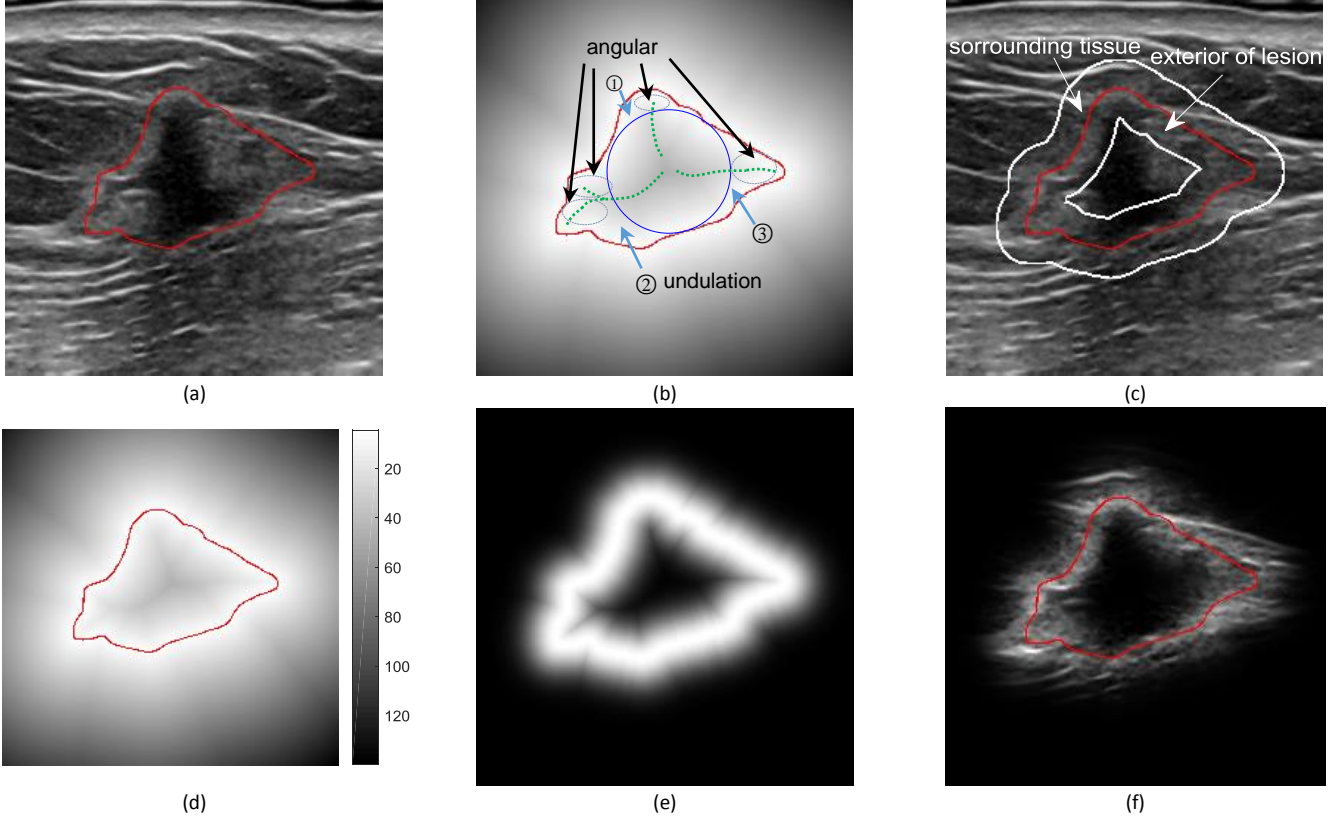


Fig. 2. An example of BIRADS-oriented feature map for capturing lesion characteristics: (a) A malignant lesion with boundary (red line); (b) Undulation and angular characteristics: the number of significant lobulated areas, and the number of the local maxima on the distance map; (c) Abrupt degree: the average gray intensities of the surrounding tissue and the lesion's exterior; (d) The distance map is represented by the grayscale, in which the lighter the gray, the smaller the distance to the boundary; (e) DTGF: A distance-transformation coupled Gaussian filter with $\sigma = 20$; (f) BFM: The BIRADS feature map with $\sigma = 20$.

C. SCAE Neural Network

A stacked convolutional auto-encoder (SCAE) neural network follows an unsupervised encoder-decoder learning paradigm [22, 25]. A standard auto-encoder (AE) is a three-layer network that attempts to output an approximation of the input with an encoder and a decoder. The encoder maps the input $\{\mathbf{x}^{(n)} \in \mathbb{R}^d\}_{n=1}^N$ to a hidden feature representation vector $\mathbf{h} \in \mathbb{R}^{d'}$ through a nonlinear projection function (activation function) $\mathbf{f}_{en}(\cdot)$:

$$\mathbf{h} = \mathbf{f}_{en}(\mathbf{W}_{en} \cdot \mathbf{x} + \mathbf{b}_{en}) \quad (3)$$

Then, the decoder maps the hidden feature representation \mathbf{h} to an output vector $\hat{\mathbf{x}} \in \mathbb{R}^d$:

$$\hat{\mathbf{x}} = \mathbf{f}_{de}(\mathbf{W}_{de} \cdot \mathbf{h} + \mathbf{b}_{de}) \quad (4)$$

it can be seen that the shape and boundary of the lesion are emphasized, and the undulation and angular characteristics based on the distance map are well reflected in the BFM. The converted BFM not only keep the key information from the original US image but also enhance the lesion's shape, boundary, undulation, and angular characteristics. With the guidance of the BFM, the advanced deep feature learning can focus on the clinically-assigned breast lesion characteristics.

where $\hat{\mathbf{x}}$ is expected to be an approximate reconstruction of the input \mathbf{x} . The model is learned to minimize reconstruction error:

$$\min_{\theta_r} J(\theta_r) = \frac{1}{N} \sum_{n=1}^N \text{loss}_r(\mathbf{x}^{(n)}, \hat{\mathbf{x}}^{(n)}) + \gamma \cdot \mathbf{R}(\theta_r) \quad (5)$$

where the reconstructing loss function $\text{loss}_r(\cdot)$ uses Euclidean distance $\text{loss}_r(\mathbf{x}, \hat{\mathbf{x}}) = \|\mathbf{x} - \hat{\mathbf{x}}\|_2^2$ and parameter regular term $\mathbf{R}(\theta_r) = \|\mathbf{W}_{en}\|_F^2 + \|\mathbf{W}_{de}\|_F^2$, and $\mathbf{W}_{de} = \mathbf{W}_{en}^T$.

Convolutional AE (CAE) [26] is an extension of the standard AE that introduces a convolution operation between hierarchical connections. Unlike standard AE, the inputs of CAE are not restricted to one-dimensional vectors but can also be 2D images. CAE captures structural information and preserves the local spatiality of an image by sharing weights among all input locations. Similar to CNN, the hidden feature map \mathbf{h} is given by

$$\mathbf{h} = \mathbf{f}_{en}(\mathbf{W}_{en} * \mathbf{x} + \mathbf{b}_{en}) \quad (6)$$

With the feature maps, the reconstruction of input is obtained using

$$\hat{\mathbf{x}} = \mathbf{f}_{de}(\mathbf{W}_{de} * \mathbf{h} + \mathbf{b}_{de}) \quad (7)$$

where $*$ denotes the 2D convolution.

A SCAE network is formed by stacking several CAEs hierarchically. The input of the $i+1$ -th layer is the feature map of the i -th layer:

$$\begin{cases} \mathbf{h}^l = \mathbf{f}_{en}^l(\mathbf{W}_{en}^l * \mathbf{h}^{l-1} + \mathbf{b}_{en}^l) \\ \mathbf{h}^1 = \mathbf{f}_{en}^1(\mathbf{W}_{en}^1 * \mathbf{x} + \mathbf{b}_{en}^1) \end{cases} \quad (8)$$

where $l = 2, \dots, L$. The whole network is unsupervised trained in a greedy, layer-wised fashion by minimizing the reconstruction error of its input. Once all layers have been trained, a minimized reconstruction error means that the feature maps from the output of the encoder contain the most important information from the input. The traditional SCAE-based classifier includes two detached stages: 1. Unsupervised learning for image reconstruction; 2. Fine-tuning the classification network only with supervised learning. After stage 1 has finished, the classification stage removes the decoder and only preserves the input and the encoder. The output of the encoder is then fed into a softmax classifier or other classifiers with supervised training. The classic methods [26] learn the softmax classifier or fine-tune the parameters of all the layers together with the labeled samples as inputs.

D. BIRADS-SDL Neural Network

As mentioned in Section II-C, representative features from a standard SCAE are learned mainly for image reconstruction. The final stage fine-tuned the parameters with supervised learning may have a limited impact on the classification task. More importantly, it is difficult to learn an effective CNN model directly with a small number of labeled samples.

Inspired by the multi-task network [27], we developed a novel BIRADS-SDL network, as shown in Fig. 1. Let $\{\mathbf{x}^{(n)}, \mathbf{y}^{(n)}\}_{n=1}^N$ be the labeled samples. $\mathbf{y} \in \mathfrak{R}^K$ is a one-hot label vector. The lesion classification task is implemented by an encoder network and a classifier, as shown in Fig. 1, which can be expressed as

$$\begin{cases} \mathbf{h} = \mathbf{f}_{en}(\mathbf{W}_{en} * \mathbf{x} + \mathbf{b}_{en}) \\ \hat{\mathbf{y}} = \mathbf{f}_c(\mathbf{h}, \boldsymbol{\beta}) \end{cases} \quad (9)$$

where \mathbf{h} is the output of the encoder, $\mathbf{f}_c(\cdot)$ is a softmax classifier, and $\boldsymbol{\beta}$ is a vector of parameters of the classifier to be learned. $\hat{\mathbf{y}} \in \mathfrak{R}^K$ is the output of the classifier and ranges within $[0, 1]$. The objective function of classification is

$$\min_{\boldsymbol{\theta}_c} J(\boldsymbol{\theta}_c) = \frac{1}{N} \sum_{n=1}^N \text{loss}_c(\mathbf{y}^{(n)}, \hat{\mathbf{y}}^{(n)}) + \gamma \cdot \mathbf{R}(\boldsymbol{\theta}_c) \quad (10)$$

where $\boldsymbol{\theta}_c = [\mathbf{W}_{en}, \mathbf{b}_{en}; \boldsymbol{\beta}]$ is learning or tuning by the training dataset. Commonly, the loss function $\text{loss}_c(\cdot)$ uses cross-entropy:

$$\text{loss}_c(\mathbf{y}, \hat{\mathbf{y}}) = - \sum_{k=1}^K \delta(\mathbf{y}(k) = 1) \cdot \log(\hat{\mathbf{y}}(k)) \quad (11)$$

where $\delta(\cdot)$ is an indicative function (the value is 1 if $\mathbf{y}(k)$ is equal to 1), and K is the number of classes. Here, $K = 2$ because the lesion is either benign or malignant.

The image reconstruction pipeline is similar to the standard SCAE structure and consists of an encoder and a decoder, as shown in Fig. 1. Combined with the reconstruction pipeline, the objective function of the BIRADS-SDL network is as follows:

$$\min_{\boldsymbol{\theta}} J(\boldsymbol{\theta}) = \frac{1}{N} \sum_{n=1}^N \lambda \cdot \text{loss}_c(\mathbf{y}^{(n)}, \hat{\mathbf{y}}^{(n)}) + (1 - \lambda) \cdot \text{loss}_r(\mathbf{x}^{(n)}, \hat{\mathbf{x}}^{(n)}) + \gamma \cdot \mathbf{R}(\boldsymbol{\theta}) \quad (12)$$

where $\boldsymbol{\theta} = [\mathbf{W}_{en}, \mathbf{b}_{en}; \mathbf{W}_{de}, \mathbf{b}_{de}; \boldsymbol{\beta}]$ and $\lambda \in [0, 1]$ is used to balance the classification and reconstruction tasks. The objective function is a convex optimization problem and can be achieved by alternative learning [27]. During feature learning, the encoding parameters are shared among both tasks, while the decoding parameters only participate in the reconstruction task.

In this paper, the classification pipeline has four convolutional layers: 8(Conv1), 16(Conv2), 32(Conv3), and 64(Conv4) @3×3 filters respectively, four max-pooling layers of size 2×2 after each convolutional layer, and three fully-connected layers (FC1, FC2, FC3), as shown in Fig. 1. The number of neurons in FC1 and FC2 is 256 and 64, respectively. The output layer FC3 has a softmax activation function with two neurons. The dropout (with a probability of 0.5) is applied after FC1 and FC2 to prevent overfitting. ReLU activations are used in all hidden layers. The reconstruction pipeline has an encoder and a decoder. The encoder is shared with the classification pipeline, including the four convolutional layers (Conv1, Conv2, Conv3, and Conv4) and two fully-connected layers (FC1 and FC2). The decoder has the inverse configuration of the encoder, including two fully-connected layers (FC4 and FC5), four pairs of convolution and upsampling layers, and a convolutional output layer with linear activations. The classification and reconstruction tasks are alternately updated via Adam with a learning rate of 3×10^{-4} and the parameter λ equal to 0.5, stopping to update the network when the average reconstruction loss remains stable.

III. EXPERIMENTAL SETUP

A. Data Set I — Public UDIAT

We used a public breast B-Mode US image dataset, named UDIAT [28], to investigate the effect of the proposed methods. UDIAT contains 163 images collected in the UDIAT Diagnostic Centre of the Parc Taulí Corporation, Sabadell, Spain with a Siemens ACUSON Sequoia C512 system 17L5 HD linear array transducer (8.5 MHz). The average size of the images is 760×570 pixels, with a nominal pixel size of 0.084mm. Lesions were delineated by an experienced

radiologist. In this study, 160 images with lesion sizes smaller than 256×256 pixels were selected and cropped to 256×256 centered on the lesions. These 160 images include 53 images with malignant lesions and 107 with benign lesions.

B. Data Set II — In-house Clinical Dataset

The in-house clinical dataset, named UTSW dataset, is a B-mode US breast image dataset collected at the University of Texas Southwestern Medical Center with a Philips iU22 scanner (Philips Medical Systems, equipped with a 12-5 MHz linear array transducer). The average size of the images is 870×660 pixels, with pixel size varying from 0.04 to 0.1mm (average pixel size is 0.068mm). The lesions were identified as benign or malignant based on the pathologic examination of a subsequent biopsy. Lesions on the images were marked with two or four boundary points. In this study, we selected 295 images from 144 patients, including 205 benign lesions and 90 malignant lesions. The images were resampled to a resolution of 0.084mm and cropped to 256×256 centered on the lesions. A marker-controlled watershed segmentation method was used to create the tumor boundary [29].

C. Experiments Setup

We designed five scenarios to evaluate BIRADS-SDL's performance within and across the two datasets: 1) within the UDIAT dataset, 50% of the samples were randomly selected from benign and malignant lesions to form the training set, and the remaining 50% were used as the testing set; 2) within the UTSW dataset, 80% per class of samples were randomly chosen to construct a training set, and 20% of the samples were randomly chosen as the test set; 3) 50% of the samples selected from the UDIAT were used as the training set, and 20% of the samples from the UTSW dataset were selected as the testing set; 4) 80% of the samples selected from the UTSW dataset were used as the training set, and 50% samples from UDIAT served as the testing set; and 5) a combined training set was constructed from 50% of the samples from UDIAT and 80% of samples from UTSW dataset, and the remaining samples from each dataset were used as two testing sets. In the experiments, the gray values of pixels were normalized to [0, 1]. All algorithms were executed using Python in the environment of an Intel Xeon CPU E5-1603@2.80 GHz and 32 GB of RAM.

D. Performance Metric

In this paper, ACC, AUC, SEN, SPE, PPV, NPV, and MCC represent seven performance metrics: accuracy, area the under receiver operating characteristic curve, sensitivity, specificity, positive predictive value, negative predictive value, and Matthews correlation coefficient [30], respectively [31]. In the experiments, TP is the number of true positives (malignant breast tumor), FN is the number of false negatives (benign breast tumor), TN is the number of true negatives, and FP is the number of false positives.

$$\begin{aligned} \text{SEN} &= \text{TP}/(\text{TP} + \text{FN}) \\ \text{SPE} &= \text{TN}/(\text{FP} + \text{TN}) \\ \text{PPV} &= \text{TP}/(\text{TP} + \text{FP}) \end{aligned} \quad (13)$$

$$\begin{aligned} \text{NPV} &= \text{TN}/(\text{TN} + \text{FN}) \\ \text{ACC} &= (\text{TP} + \text{TN})/(\text{TP} + \text{FP} + \text{FN} + \text{TN}) \\ \text{AUC} &= 0.5 \cdot (\text{TP}/(\text{TP} + \text{FN}) + \text{TN}/(\text{TN} + \text{FP})) \\ \text{MCC} &= \frac{\text{TP} \cdot \text{TN} - \text{FP} \cdot \text{FN}}{\sqrt{(\text{TP} + \text{FN})(\text{TP} + \text{FP})(\text{TN} + \text{FN})(\text{TN} + \text{FP})}} \end{aligned}$$

ACC measures the ratio of the number of samples correctly classified to the total number of samples. AUC indicates the trade-off between SEN and SPE, whose advantages are the robust description of the classifier's predictive ability. MCC gives a better evaluation than ACC when the numbers of negative samples and positive samples are unequal. The larger the value is, the better the performance of the classifier.

IV. EXPERIMENTAL RESULTS AND DISCUSSION

A. Classification Results on Single Dataset

To demonstrate the effectiveness of BIRADS-SDL, we chose three SCAE-based methods for comparisons: 1) ORI-SCAE, which uses original images as inputs and a standard SCAE network with unsupervised learning for reconstruction, then adds three fully-connected layers (FC1, FC2, FC3) for diagnosis prediction. Fine-tuning with the labeled samples is performed on the whole network; 2) BIRADS-SCAE, which is similar to ORI-SCAE, but it uses with BFM as the network inputs; and 3) ORI-SDL, a semi-supervised learning method, like BIRADS-SDL, that uses original images, not BFM, as inputs.

TABLE I
CLASSIFICATION RESULTS (MEAN \pm STD %) FOR DIFFERENT METHODS WHEN TRAINING AND TESTING ON UDIAT. BOLD INDICATES THE BEST RESULTS

| Method | ORI-SCAE | ORI-SDL | BIRADS-SCAE | BIRADS-SDL |
|--------|-------------------|------------------|------------------|----------------------------------|
| ACC | 84.25 \pm 4.61 | 86.87 \pm 2.57 | 89.38 \pm 3.13 | 92.00\pm2.38 |
| AUC | 79.75 \pm 5.96 | 81.93 \pm 2.95 | 86.23 \pm 3.82 | 88.98\pm2.51 |
| MCC | 64.33 \pm 11.27 | 69.02 \pm 5.73 | 75.79 \pm 6.87 | 82.07\pm5.02 |
| SEN | 64.84 \pm 10.17 | 68.51 \pm 6.02 | 76.65 \pm 6.96 | 79.64\pm4.27 |
| SPE | 94.65 \pm 2.71 | 95.34 \pm 2.96 | 95.82 \pm 2.45 | 98.32\pm1.73 |
| PPV | 86.16 \pm 7.95 | 88.12 \pm 6.10 | 90.38 \pm 5.17 | 95.96\pm4.35 |
| NPV | 83.48 \pm 4.67 | 86.61 \pm 2.38 | 88.94 \pm 3.30 | 90.47\pm2.83 |

TABLE II
CLASSIFICATION RESULTS (MEAN \pm STD %) FOR DIFFERENT METHODS WHEN TRAINING AND TESTING ON UTSW DATASET.

| Method | ORI-SCAE | ORI-SDL | BIRADS-SCAE | BIRADS-SDL |
|--------|-------------------|-------------------|-----------------------------------|----------------------------------|
| ACC | 81.69 \pm 4.07 | 82.03 \pm 4.17 | 82.54 \pm 4.42 | 83.90\pm3.81 |
| AUC | 74.62 \pm 5.40 | 75.02 \pm 6.02 | 72.58 \pm 8.45 | 79.62\pm3.48 |
| MCC | 54.83 \pm 8.25 | 55.56 \pm 10.19 | 53.25 \pm 13.66 | 60.73\pm6.88 |
| SEN | 56.50 \pm 12.53 | 56.29 \pm 12.35 | 49.79 \pm 17.86 | 69.96\pm8.09 |
| SPE | 92.75 \pm 3.46 | 93.74 \pm 2.84 | 95.38\pm3.11 | 89.29 \pm 5.79 |
| PPV | 78.68 \pm 4.32 | 79.29 \pm 9.19 | 82.57\pm11.73 | 74.56 \pm 8.48 |
| NPV | 82.88 \pm 5.31 | 82.81 \pm 5.80 | 82.58 \pm 5.58 | 87.94\pm3.39 |

Table I shows the classification results (mean \pm standard

deviation %) for the four methods on the UDIAT dataset. First, comparing the methods with different inputs (ORI-SCAE and BIRADS-SCAE, ORI-SDL and BIRADS-SDL), we found that BIRADS-based methods outperformed ORI-based methods from the perspective of the seven metrics. The BIRADS-based methods achieved ACC, AUC, and MCC values about 5%, 7%, and 10% higher, respectively, than the ORI-based methods, which indicates the advantage of using BIRADS-oriented feature maps. Second, comparing ORI-SDL to ORI-SCAE and BIRADS-SDL to BIRADS-SCAE, we found that the SDL-based methods (ORI-SDL and BIRADS-SDL) obtained better results than the methods with the fine-tuning strategy (ORI-SCAE and BIRADS-SCAE), which means they learn more effective features for classification using unsupervised image reconstruction with the constraints from the lesion classification task. Overall, the proposed BIRADS-SDL produces the best diagnosis results by taking advantage of BIRADS features and SDL with small datasets.

Similar conclusions can be drawn from the classification results on the UTSW dataset, shown in Table II. BIRADS-SDL outperformed the other three compared methods in terms of MCC, ACC, and AUC. Unlike the UDIAT dataset, BIRADS-SDL only outperformed the other methods in terms of ACC by about 1%~2%. One reason for this might be that the lesion boundary produced by auto-segmentation is not accurate, which would reduce the classification accuracy. However, BIRADS-SDL achieved a much higher SEN than the other methods. Moreover, BIRADS-SDL outperformed the other methods in terms of MCC and AUC by about 5%. This indicates that the proposed BIRADS-SDL achieves a better balance between SEN and SPE than the other methods.

TABLE III

CLASSIFICATION RESULTS (MEAN \pm STD %) FOR DIFFERENT METHODS WHEN TRAINING ON UTSW DATASET AND TESTING ON UDIAT.

| Method | ORI-SCAE | ORI-SDL | BIRADS-SCAE | BIRADS-SDL |
|--------|----------------------------------|----------------------------------|------------------|-----------------------------------|
| ACC | 75.00 \pm 2.30 | 77.25 \pm 3.00 | 77.47 \pm 2.73 | 79.25\pm3.36 |
| AUC | 68.63 \pm 2.65 | 71.20 \pm 2.92 | 68.30 \pm 3.93 | 70.82\pm3.32 |
| MCC | 39.32 \pm 4.49 | 46.46 \pm 5.75 | 42.75 \pm 6.01 | 50.86\pm7.58 |
| SEN | 51.59 \pm 6.43 | 52.71\pm5.54 | 44.49 \pm 9.44 | 45.95 \pm 5.06 |
| SPE | 85.66 \pm 2.62 | 89.68 \pm 2.58 | 92.10 \pm 2.51 | 95.68\pm2.27 |
| PPV | 61.96 \pm 4.01 | 72.00 \pm 5.90 | 71.21 \pm 5.79 | 84.11\pm 7.35 |
| NPV | 79.63\pm3.52 | 79.00 \pm 3.95 | 79.16 \pm 4.14 | 78.11 \pm 3.27 |

B. Model Validation across Dataset

Table III and IV summarize the classification results across datasets with the same comparison as described in Section IV-A. Table III shows the classification results for each method trained on the UTSW dataset (randomly selected 80% of the samples) and tested on UDIAT (randomly selected 50% of the samples). The classification accuracy of all the methods was lower than in Table I. One possible reason is that two datasets collected by different manufacturers' devices have different characteristics. Another reason might be that the model trained on the UTSW dataset has limited generalizability due to the

limited samples and imprecise lesion segmentation. Table IV shows the classification results for each method trained on UDIAT (randomly selected 50% of the samples) and tested on the UTSW dataset (randomly selected 20% of the samples). BIRADS-SDL yielded results similar to those in Table II.

TABLE IV

CLASSIFICATION RESULTS (MEAN \pm STD %) FOR DIFFERENT METHODS WHEN TRAINING ON UDIAT AND TESTING ON UTSW DATASET.

| Method | ORI-SCAE | ORI-SDL | BIRADS-SCAE | BIRADS-SDL |
|--------|-------------------|-----------------------------------|----------------------------------|-----------------------------------|
| ACC | 74.07 \pm 3.04 | 77.97 \pm 5.67 | 74.92 \pm 4.14 | 79.49\pm5.38 |
| AUC | 63.98 \pm 5.65 | 65.46 \pm 5.29 | 74.95\pm5.40 | 73.01 \pm 5.88 |
| MCC | 30.48 \pm 11.50 | 42.24 \pm 13.98 | 47.06 \pm 10.35 | 49.83\pm10.71 |
| SEN | 41.40 \pm 11.65 | 34.80 \pm 8.71 | 75.11\pm9.91 | 55.64 \pm 11.69 |
| SPE | 86.56 \pm 3.55 | 96.13\pm3.54 | 74.80 \pm 4.07 | 90.38 \pm 3.90 |
| PPV | 54.06 \pm 11.25 | 80.25\pm17.24 | 57.58 \pm 8.90 | 72.41 \pm 7.61 |
| NPV | 79.33 \pm 2.85 | 77.87 \pm 5.04 | 86.84\pm4.24 | 81.87 \pm 6.20 |

Further, each method was trained on the combined UDIAT (randomly selected 50% of the samples) and UTSW datasets (randomly selected 80% of the samples), then tested on the remaining samples from each dataset, respectively. Table V and VI summarize the classification results for each method. It can be seen that all the methods produced results similar to those shown in Table I and II, and the proposed BIRADS-SDL performed the best in all the comparisons. This indicates that, among the methods compared, BIRADS-SDL method is more generalizable across different datasets without overfitting to single institution data.

TABLE V

CLASSIFICATION RESULTS (MEAN \pm STD %) FOR DIFFERENT METHODS WHEN TRAINING ON A COMBINED UDIAT AND UTSW DATASET AND TESTING ON UDIAT.

| Method | ORI-SCAE | ORI-SDL | BIRADS-SCAE | BIRADS-SDL |
|--------|------------------|------------------|------------------|----------------------------------|
| ACC | 85.42 \pm 2.12 | 85.62 \pm 2.58 | 89.46 \pm 2.20 | 91.50\pm2.29 |
| AUC | 79.61 \pm 3.25 | 81.79 \pm 3.10 | 86.04 \pm 3.23 | 88.28\pm2.76 |
| MCC | 65.75 \pm 5.48 | 68.09 \pm 5.66 | 75.99 \pm 5.41 | 80.92\pm5.33 |
| SEN | 63.16 \pm 7.08 | 68.59 \pm 6.29 | 75.81 \pm 7.20 | 78.49\pm4.60 |
| SPE | 96.06 \pm 2.41 | 94.99 \pm 2.86 | 96.28 \pm 2.89 | 98.08\pm1.71 |
| PPV | 88.56 \pm 7.34 | 88.26 \pm 6.50 | 91.23 \pm 5.47 | 95.63\pm4.08 |
| NPV | 84.64 \pm 2.91 | 84.78 \pm 3.36 | 88.95 \pm 3.22 | 89.92\pm2.05 |

TABLE VI

CLASSIFICATION RESULTS (MEAN \pm STD %) FOR DIFFERENT METHODS WHEN TRAINING ON A COMBINED UDIAT AND UTSW DATASET AND TESTING ON UTSW DATASET.

| Method | ORI-SCAE | ORI-SDL | BIRADS-SCAE | BIRADS-SDL |
|--------|-------------------|-----------------------------------|------------------|-----------------------------------|
| ACC | 78.69 \pm 5.11 | 81.36 \pm 4.79 | 82.08 \pm 4.61 | 82.49\pm2.88 |
| AUC | 69.49 \pm 4.86 | 73.92 \pm 5.60 | 74.83 \pm 4.13 | 78.12\pm4.49 |
| MCC | 47.05 \pm 10.82 | 55.61 \pm 8.46 | 55.67 \pm 9.40 | 57.31\pm6.42 |
| SEN | 45.80 \pm 9.28 | 52.84 \pm 12.87 | 56.89 \pm 7.55 | 67.13\pm11.23 |
| SPE | 93.17 \pm 6.19 | 94.99\pm3.79 | 92.77 \pm 5.38 | 89.12 \pm 4.62 |
| PPV | 78.14 \pm 12.42 | 84.83\pm10.24 | 79.51 \pm 8.49 | 71.68 \pm 9.10 |
| NPV | 79.31 \pm 4.05 | 80.89 \pm 6.27 | 83.04 \pm 3.55 | 87.17\pm4.92 |

Finally, all models were pre-trained on the UTSW dataset, and the whole network was fine-tuned with 50% of the samples from UDIAT, and then the models were tested on the remaining UDIAT images, as shown in Table VII. Compared with the results in Table I, there is no obvious difference in the evaluation metrics. We observed the changes of the loss function during training the models, as shown in Fig. 3. It can be seen that the loss values of image reconstruction decrease rapidly with the iteration until it is relatively stable. The reconstruction losses of BIRADS-SDL with the pre-trained strategy (transfer BIRADS-SDL) are smaller than the losses of BIRADS-SDL, and the convergence speed is faster. The losses of image classification show a similar trend. A pre-trained model can help BIRADS-SDL speed up convergence and achieve smaller losses of image reconstruction.

TABLE VII
CLASSIFICATION RESULTS (MEAN \pm STD %) OF EACH METHOD (PRE-TRAINED WITH UTSW DATASET AND FINE-TUNED WITH TRAINING DATASET OF UDIAT) ON THE TEST SET OF UDIAT

| Method | ORI-SCAE | ORI-SDL | BIRADS-SCAE | BIRADS-SDL |
|--------|------------------|------------------|------------------|----------------------------------|
| ACC | 84.86 \pm 1.61 | 85.28 \pm 2.62 | 89.12 \pm 2.74 | 91.09\pm1.92 |
| AUC | 80.67 \pm 2.12 | 81.15 \pm 2.93 | 85.59 \pm 4.56 | 88.99\pm2.50 |
| MCC | 65.26 \pm 3.21 | 67.08 \pm 6.09 | 73.85 \pm 7.71 | 79.69\pm4.59 |
| SEN | 67.80 \pm 5.39 | 67.36 \pm 5.45 | 76.52 \pm 9.88 | 82.71\pm4.56 |
| SPE | 93.55 \pm 2.10 | 94.94 \pm 3.20 | 94.66 \pm 3.28 | 95.27\pm1.32 |
| PPV | 84.28 \pm 4.16 | 87.86 \pm 7.36 | 86.43 \pm 8.30 | 89.82\pm3.28 |
| NPV | 85.22 \pm 2.76 | 84.46 \pm 3.16 | 90.37 \pm 3.86 | 91.63\pm2.10 |

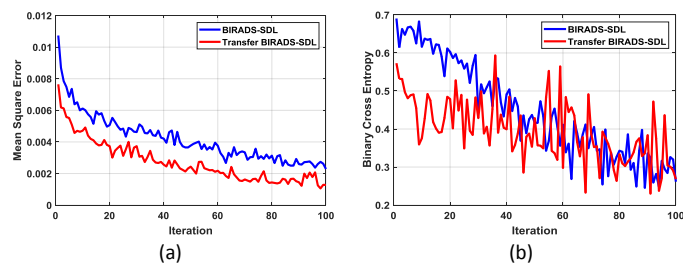


Fig. 3. The loss values of BIRADS-SDL and transfer BIRADS-SDL during training on UDIAT: (a) the loss of image reconstruction; (b) the loss of classification.

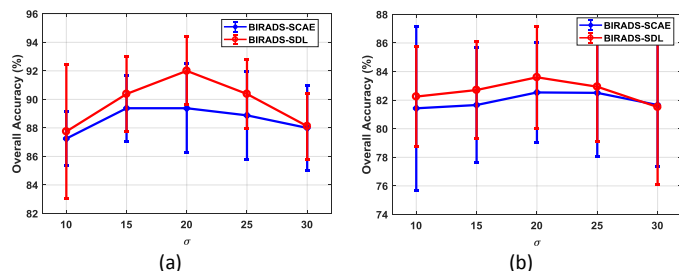


Fig. 4. Effect of parameter σ in a Gaussian filter on BIRADS-based methods for (a) UDIAT and (b) UTSW dataset.

C. Effects of Gaussian Filter Parameter σ

Fig. 4 shows the variations in the overall accuracy of classification results for the two BIRADS-based methods across σ values. It can be seen that BIRADS-SDL has higher

accuracy than BIRADS-SCAE across almost every σ value, though it has some fluctuations. All curves show the best result when $\sigma = 20$ and decrease slightly with smaller or larger σ values. It also can be seen that the standard deviation variations are relatively small, around $\sigma = 20$. This indicates that the area across the lesion boundary within a certain range plays an important role in diagnosis and should be given more attention.

V. DISCUSSION AND CONCLUSION

We developed a novel BIRADS-SDL network to incorporate clinically-assigned breast lesion characteristics into a task-oriented semi-supervised deep learning method for accurate diagnosis on US images with a relatively small training dataset. We verified the effectiveness of BIRADS-SDL on two breast US image datasets and found that the network achieved high diagnostic accuracy. In the public UDIAT dataset, the BIRADS-SDL network trained with 80 images achieved the highest ACC and AUC values of 92% and 89%, respectively. In the in-house clinical dataset, we obtained ACC and AUC values of 84% and 79%, respectively.

Unlike those traditional machine learning methods [32], the proposed BIRADS-SDL method automatically learned representative and discriminative features by hierarchical deep neural network. Different from the recent DL methods with pre-training techniques or transfer learning [24, 33, 34], we fuse the existing conventional BIRADS features into a semi-supervised deep neural network which improves performance in breast lesion diagnosis. In our case, the ACC value of BIRADS-SDL was higher than the highest ACC value of the previous transfer DL method [34], 92% vs. 84%; and the BIRADS-SDL only used 80 labeled images for training the network and achieved an AUC (~89%) comparable to the results reported in recent papers [24, 33], where the AUC values are around 85% and the networks are trained on bigger datasets.

We evaluated the generalizability of BIRADS-SDL with experiments across two datasets collected from two different institution/and US devices. When training the model on both datasets together, the developed BIRADS-SDL is generalizable across the different US devices and institutions without overfitting to a single dataset and achieved satisfactory results. Although the model was learned from one dataset and was tested on a different dataset, it still performed better than three comparable networks.

There were several limitations to our study. BIRADS-SDL requires accurate lesion segmentation to convert original breast US images to BFMs. The ACC and AUC values obtained on UTSW dataset might be lower than the values obtained on UDIAT because the boundaries of the lesions produced by auto-segmentation are not accurate. Furthermore, our method does not take into account the relationship between lesion images with multiple different angles from the same patient. In the future, we will develop an end-to-end semi-supervised breast US diagnosis ensemble system that includes lesion segmentation and classification, which will not only fuse the

clinical lesion characteristics but also use multiple US images from the same patient to make a joint decision.

In summary, the proposed BIRADS-SDL achieves the best results among the compared methods in each case and has the capacity to deal with multiple different datasets under one model, thereby indicating that BIRADS-SDL is a promising method for effective breast US lesion CAD using small datasets.

ACKNOWLEDGMENT

The authors are grateful for the support in preparing the manuscript provided by Dr. Jonathan Feinberg.

REFERENCES

- [1] H.-D. Cheng, J. Shan, W. Ju, Y. Guo, and L. Zhang, "Automated breast cancer detection and classification using ultrasound images: A survey," *Pattern recognition*, vol. 43, pp. 299-317, 2010.
- [2] F. M. Osman and M. H. Yap, "The effect of filtering algorithms for breast ultrasound lesions segmentation," *Informatics in Medicine Unlocked*, 2018.
- [3] J. A. Baker and M. S. Soo, "Breast US: assessment of technical quality and image interpretation," *Radiology*, vol. 223, pp. 229-238, 2002.
- [4] G. Rizzatto, "Towards a more sophisticated use of breast ultrasound," *European radiology*, vol. 11, pp. 2425-2435, 2001.
- [5] K.-H. Hwang, J. G. Lee, J. H. Kim, H.-J. Lee, K.-S. Om, M. Yoon, *et al.*, "Computer aided diagnosis (CAD) of breast mass on ultrasonography and scintimammography," in *Enterprise networking and Computing in Healthcare Industry, 2005. HEALTHCOM 2005. Proceedings of 7th International Workshop on*, 2005, pp. 187-189.
- [6] Q. Huang, F. Zhang, and X. Li, "Machine Learning in Ultrasound Computer-Aided Diagnostic Systems: A Survey," *BioMed research international*, vol. 2018, 2018.
- [7] K. Horsch, M. L. Giger, L. A. Venta, and C. J. Vyborny, "Automatic segmentation of breast lesions on ultrasound," *Medical Physics*, vol. 28, pp. 1652-1659, 2001.
- [8] J. A. Noble and D. Boukerroui, "Ultrasound image segmentation: a survey," *IEEE Transactions on medical imaging*, vol. 25, pp. 987-1010, 2006.
- [9] W.-C. Shen, R.-F. Chang, W. K. Moon, Y.-H. Chou, and C.-S. Huang, "Breast ultrasound computer-aided diagnosis using BI-RADS features," *Academic radiology*, vol. 14, pp. 928-939, 2007.
- [10] W. G. Flores, W. C. de Albuquerque Pereira, and A. F. C. Infantosi, "Improving classification performance of breast lesions on ultrasonography," *Pattern Recognition*, vol. 48, pp. 1125-1136, 2015.
- [11] C. D'orsi, L. Bassett, and S. Feig, "Breast imaging reporting and data system (BI-RADS)," *Breast imaging atlas, 4th edn. American College of Radiology, Reston Google Scholar*, 1998.
- [12] N. Akhtar and A. Mian, "Threat of adversarial attacks on deep learning in computer vision: A survey," *arXiv preprint arXiv:1801.00553*, 2018.
- [13] Y. Bengio, A. Courville, and P. Vincent, "Representation learning: A review and new perspectives," *IEEE transactions on pattern analysis and machine intelligence*, vol. 35, pp. 1798-1828, 2013.
- [14] Y. Guo, Y. Liu, A. Oerlemans, S. Lao, S. Wu, and M. S. Lew, "Deep learning for visual understanding: A review," *Neurocomputing*, vol. 187, pp. 27-48, 2016.
- [15] Y. LeCun, Y. Bengio, and G. Hinton, "Deep learning," *nature*, vol. 521, p. 436, 2015.
- [16] J. Schmidhuber, "Deep learning in neural networks: An overview," *Neural networks*, vol. 61, pp. 85-117, 2015.
- [17] G. Litjens, T. Kooi, B. E. Bejnordi, A. A. A. Setio, F. Ciompi, M. Ghafoorian, *et al.*, "A survey on deep learning in medical image analysis," *Medical image analysis*, vol. 42, pp. 60-88, 2017.
- [18] D. Shen, G. Wu, and H.-I. Suk, "Deep learning in medical image analysis," *Annual review of biomedical engineering*, vol. 19, pp. 221-248, 2017.
- [19] D. Wang, A. Khosla, R. Gargeya, H. Irshad, and A. H. Beck, "Deep learning for identifying metastatic breast cancer," *arXiv preprint arXiv:1606.05718*, 2016.
- [20] O. Ronneberger, P. Fischer, and T. Brox, "U-net: Convolutional networks for biomedical image segmentation," in *International Conference on Medical image computing and computer-assisted intervention*, 2015, pp. 234-241.
- [21] L. Hou, D. Samaras, T. M. Kurc, Y. Gao, J. E. Davis, and J. H. Saltz, "Patch-based convolutional neural network for whole slide tissue image classification," in *Proceedings of the IEEE Conference on Computer Vision and Pattern Recognition*, 2016, pp. 2424-2433.
- [22] J.-Z. Cheng, D. Ni, Y.-H. Chou, J. Qin, C.-M. Tiu, Y.-C. Chang, *et al.*, "Computer-aided diagnosis with deep learning architecture: applications to breast lesions in US images and pulmonary nodules in CT scans," *Scientific reports*, vol. 6, p. 24454, 2016.
- [23] S. Han, H.-K. Kang, J.-Y. Jeong, M.-H. Park, W. Kim, W.-C. Bang, *et al.*, "A deep learning framework for supporting the classification of breast lesions in ultrasound images," *Physics in Medicine & Biology*, vol. 62, p. 7714, 2017.
- [24] N. Antropova, B. Q. Huynh, and M. L. Giger, "A deep feature fusion methodology for breast cancer diagnosis demonstrated on three imaging modality datasets," *Medical physics*, vol. 44, pp. 5162-5171, 2017.
- [25] L. Gondara, "Medical image denoising using convolutional denoising autoencoders," in *Data Mining Workshops (ICDMW), 2016 IEEE 16th International Conference on*, 2016, pp. 241-246.
- [26] J. Masci, U. Meier, D. Cireřan, and J. Schmidhuber, "Stacked convolutional auto-encoders for hierarchical feature extraction," in *International Conference on Artificial Neural Networks*, 2011, pp. 52-59.
- [27] M. Ghifary, W. B. Kleijn, M. Zhang, D. Balduzzi, and W. Li, "Deep reconstruction-classification networks for unsupervised domain adaptation," in *European Conference on Computer Vision*, 2016, pp. 597-613.
- [28] M. H. Yap, G. Pons, J. Martí, S. Ganau, M. Sentís, R. Zwigelaar, *et al.*, "Automated breast ultrasound lesions detection using convolutional neural networks," *IEEE journal of biomedical and health informatics*, vol. 22, pp. 1218-1226, 2018.
- [29] W. Gomez, L. Leija, A. Alvarenga, A. Infantosi, and W. Pereira, "Computerized lesion segmentation of breast ultrasound based on marker-controlled watershed transformation," *Medical physics*, vol. 37, pp. 82-95, 2010.
- [30] D. M. Powers, "Evaluation: from precision, recall and F-measure to ROC, informedness, markedness and correlation," 2011.
- [31] H. Zhou, M. Gao, and J. Skolnick, "ENTPRISE: an algorithm for predicting human disease-associated amino acid substitutions from sequence entropy and predicted protein structures," *PLOS one*, vol. 11, p. e0150965, 2016.
- [32] A. Jalalian, S. B. Mashohor, H. R. Mahmud, M. I. B. Saripan, A. R. B. Ramli, and B. Karasfi, "Computer-aided detection/diagnosis of breast cancer in mammography and ultrasound: a review," *Clinical imaging*, vol. 37, pp. 420-426, 2013.
- [33] M. Byra, "Discriminant analysis of neural style representations for breast lesion classification in ultrasound," *Biocybernetics and Biomedical Engineering*, 2018.
- [34] M. Byra, M. Galperin, H. Ojeda-Fournier, L. Olson, M. O'Boyle, C. Comstock, *et al.*, "Breast mass classification in sonography with transfer learning using a deep convolutional neural network and color conversion," *Medical physics*, 2018.